Competing effects of inertia, sheet elasticity, fluid compressibility, and viscoelasticity on the synchronization of two actuated sheets

Cite as: Phys. Fluids **33**, 043109 (2021); https://doi.org/10.1063/5.0049099 Submitted: 01 March 2021 • Accepted: 29 March 2021 • Published Online: 21 April 2021

Chaojie Mo and Dmitry A. Fedosov







ARTICLES YOU MAY BE INTERESTED IN

Elasto-hydrodynamic interaction of two swimming spermatozoa Physics of Fluids **32**, 101901 (2020); https://doi.org/10.1063/5.0022107

An active body in a Phan-Thien and Tanner fluid: The effect of the third polar squirming mode Physics of Fluids 33, 043110 (2021); https://doi.org/10.1063/5.0048987

The physics of active polymers and filaments

The Journal of Chemical Physics 153, 040901 (2020); https://doi.org/10.1063/5.0011466

Physics of Fluids

Submit Today!

SPECIAL TOPIC: Flow and Acoustics of Unmanned Vehicles



Competing effects of inertia, sheet elasticity, fluid compressibility, and viscoelasticity on the synchronization of two actuated sheets

Cite as: Phys. Fluids **33**, 043109 (2021); doi: 10.1063/5.0049099 Submitted: 1 March 2021 · Accepted: 29 March 2021 · Published Online: 21 April 2021







Chaojie Mo and Dmitry A. Fedosov^{a)} (D)



AFFILIATIONS

Theoretical Physics of Living Matter, Institute of Biological Information Processing and Institute for Advanced Simulation, Forschungszentrum Jülich, 52425 Jülich, Germany

a) Author to whom correspondence should be addressed: d.fedosov@fz-juelich.de

ABSTRACT

Synchronization of two actuated sheets serves as a simple model for the interaction between flagellated microswimmers. Various factors, including inertia, sheet elasticity, and fluid viscoelasticity, have been suggested to facilitate the synchronization of two sheets; however, the importance of different contributions to this process still remains unclear. We perform a systematic investigation of competing effects of inertia, sheet elasticity, fluid compressibility, and viscoelasticity on the synchronization of two sheets. Characteristic time τ^s for the synchronization caused by inertial effects is inversely proportional to sheet Reynolds number Re, such that $\tau^s\omega\propto {
m Re}^{-1}$ with ω being the wave frequency. Synchronization toward stable in-phase or opposite-phase configuration of two sheets is determined by the competition of inertial effects, sheet elasticity, fluid compressibility, and viscoelasticity. Interestingly, fluid viscoelasticity results in strong synchronization forces for large beating amplitudes and Deborah numbers De > 1, which dominates over other factors and favors the in-phase configuration. Therefore, our results show that fluid viscoelasticity can dramatically enhance synchronization of microswimmers. Our investigation deciphers the importance of different competing effects for the synchronization of two actuated sheets, leading to a better understanding of interactions between microswimmers and their collective behavior.

Published under license by AIP Publishing. https://doi.org/10.1063/5.0049099

I. INTRODUCTION

Locomotion of biological and artificial microswimmers and their collective behavior have attracted considerable scientific and technological attention recently. 1-4 The foci of such studies range from physical mechanisms governing the motion and interaction of microswimmers to their use in practical applications and the emergence of collective behavior. One of the interesting aspects is the interaction between multiple swimmers facilitated by a suspending fluid medium.^{5–8} For instance, swimming spermatozoa tend to synchronize their beating flagella when they are close to each other.^{6,9-11} Even though distinct spermatozoa likely have differences in their intrinsic properties, they are able to adjust their beating characteristics (e.g., phase and frequency), and swim together as a concerted unit.9 Furthermore, synchronization of motion mediated by suspending medium is relevant to many other microswimmers, which propel using helical flagella 12,13 or cilia. 14-16

One of the first propositions that the synchronization of microswimmers is mediated by hydrodynamic interactions corresponds to the theoretical work of Taylor in 1951¹⁷ for two waving tails. Interestingly, the first experimental confirmation of the importance of hydrodynamic interactions for the synchronization of two beating flagella has been realized only a few years ago. 18 Theoretical analysis of microswimmer behavior and possible synchronization interactions is generally performed under the assumption of zero Revnolds number (i.e., no inertia), 1,17,19,20 because of non-linearity of the inertial term in the Navier-Stokes equations. Several theoretical studies have also considered the effect of fluid inertia at small Reynolds numbers.^{21,22} Even though the assumption of vanishing inertia is generally justified by the small size and low swimming velocity of microswimmers, there are examples of artificial microrobots which operate at non-negligible Reynolds numbers. 4,23,24 A theory, in which the synchronization of two inextensible waving sheets is considered, predicts no synchronization of the sheets having a front-back motion symmetry (e.g., a pure sine wave) due to kinematic reversibility of Stokes flow (i.e., under the assumption of no inertia).²⁵ Thus, synchronization is only possible if there exist additional irreversible factors which break the symmetry.^{25,26} For example, to make the synchronization of two sheets possible, a front-back asymmetry in the beating motion is proposed.^{25,27} Furthermore, other factors, such as non-negligible inertia,^{5,28,29} sheet elasticity,^{7,30} and viscoelasticity of non-Newtonian fluids,^{31,32} are sufficient to break the symmetry and enable synchronization. The 2D model of two synchronizing sheets has also been extended to small-amplitude three-dimensional beating of infinite flagellar filaments.³³

Another interesting aspect in the synchronization of two sheets is that there exist two stable synchronized configurations, namely, inphase and opposite-phase conformations with a phase difference $\phi_{\rm d}=0$ and $\phi_{\rm d}=\pi$ between the two sheets, respectively. Either the in-phase or opposite-phase configuration is stable, depending on various conditions. For instance, the geometry of a prescribed asymmetric wave determines the preference for each configuration.^{25,27} In the case of non-negligible inertial effects, the opposite-phase conformation is preferred with increasing Reynolds number.²⁸ Sheet flexibility³⁰ as well as viscoelasticity of an Oldroyd-B fluid^{31,32} drive the system toward the in-phase configuration. Noteworthy, the theory of sheet synchronization in Oldroyd-B fluids predicts the strongest synchronization force at Deborah number De of unity, while at large De, the synchronization forces asymptotically approach zero. For comparison, Deborah number of a swimming sperm in cervical mucus is larger than 100, and fluid viscoelasticity dramatically enhances clustering of bovine sperm.³⁴ Despite several existing studies on sheet synchronization, the interplay and importance of different competing effects remain unclear.

We perform a systematic analysis of the importance of different aforementioned factors for the synchronization of two sheets. Our simulations are based on the smoothed dissipative particle dynamics (SDPD) method, $^{35-37}$ a particle-based hydrodynamics technique, where both Newtonian and Oldroyd-B fluids are implemented. Two different setups are considered, including (i) a pair of inextensible waving sheets with a prescribed motion, for which synchronization forces are measured, and (ii) two flexible sheets with an internal actuation, for which dynamic synchronization toward one of the stable configurations is simulated. Our results show that for any non-zero Reynolds number Re, the two sheets always synchronize regardless of its magnitude. When inertial effects dominate, the opposite-phase configuration is preferred and a characteristic time τ^s for the synchronization normalized by the wave frequency ω is inversely proportional to Re, i.e., $\tau^s \omega \propto \text{Re}^{-1}$.

Sheet elasticity also affects stable synchronized configuration, driving the two sheets toward the in-phase configuration. Fluid compressibility favors the in-phase conformation, and might become important for millimeter-sized swimmers in highly viscous liquids. Fluid viscoelasticity, when a dominating factor, also drives the sheets toward the in-phase configuration. Nevertheless, at high enough Re, inertial effects may favor the opposite-phase conformation even in viscoelastic fluids. The modes of stable synchronized configurations with respect to different factors are summarized in Table II. Furthermore, note that the failure of the theory in Ref. 31 to predict large synchronization forces at De > 1 is related to the leading order approximation in terms of the wave amplitude. For large enough wave amplitudes, strong deviations in synchronization forces with respect to the theoretical predictions are observed for De > 1, leading to a dramatic enhancement of sheet synchronization by fluid viscoelasticity. These

results are consistent with experimental observations of the pronounced enhancement of sperm clustering in viscoelastic fluids.³⁴ In conclusion, our results provide better understanding of different competing effects for sheet synchronization and can be used to control the synchronization of artificial swimmers.

The paper is organized as follows. Section II presents fluid and sheet models, simulation setup, and the validation of these models against available theoretical predictions. In Sec. III A, synchronization of two sheets in Newtonian fluids is studied for different model parameters affecting the value of Re, fluid compressibility, and sheet flexural rigidity. Section III B presents synchronization results in Oldroyd-B viscoelastic fluids. Swimming efficiency of two synchronized sheets is discussed in Sec. III C. Finally, we conclude in Sec. IV.

II. METHODS AND MODELS

A. Viscoelastic fluid model

Fluid flow is modeled by the smoothed dissipative particle dynamics (SDPD) method, 35,36 which is a particle-based mesoscopic hydrodynamics approach. SDPD is derived through a Lagrangian discretization of the Navier–Stokes equations similar to the smoothed particle hydrodynamics (SPH) method, 38 with the proper inclusion of thermal fluctuations following the dissipative particle dynamics (DPD) approach. 39,40 We employ an SDPD version, which conserves angular momentum, 36 as it can be crucial for some problems. 41,42 In SDPD, each particle can be considered as a small fluid volume (or Lagrangian discretization point) characterized by a position r_i , velocity v_i , and mass m_i . In addition, each SDPD particle possesses a spin angular velocity ψ_i and moment of inertia I_i introduced for the enforcement of angular momentum conservation.

SDPD particles i and j interact through four pairwise forces, including conservative F_{ij}^C , dissipative F_{ij}^D , rotational F_{ij}^R , and random \tilde{F}_{ij} forces given by

$$F_{ij}^{C} = \left(\frac{\mathbf{\Pi}_{i}}{d_{i}^{2}} + \frac{\mathbf{\Pi}_{j}}{d_{j}^{2}}\right) F_{ij} \cdot \mathbf{r}_{ij},$$

$$F_{ij}^{D} = -\gamma_{ij} \left[\mathbf{v}_{ij} + (\mathbf{e}_{ij} \cdot \mathbf{v}_{ij})\mathbf{e}_{ij}\right],$$

$$F_{ij}^{R} = -\gamma_{ij} \frac{\mathbf{r}_{ij}}{2} \times (\boldsymbol{\psi}_{i} + \boldsymbol{\psi}_{j}),$$

$$\tilde{F}_{ij} = \sigma_{ij} \left(d\bar{\mathcal{W}}_{ij}^{s} + \frac{1}{3} \text{tr} \left[d\mathcal{W}_{ij}\right] \mathbf{1}\right) \cdot \frac{\mathbf{e}_{ij}}{\Delta t},$$

$$(1)$$

where $r_{ij}=r_i-r_j$, $v_{ij}=v_i-v_j$, and $e_{ij}=r_{ij}/r_{ij}$. Particle number density d_i is computed as $d_i=\sum_j W_{ij}$ using a smoothing kernel function $W_{ij}=W(r_{ij})$ that vanishes beyond a cutoff radius r_c and defines a non-negative function F_{ij} through the equation $\nabla_i W_{ij}=-r_{ij}F_{ij}$. Then, particle mass density is given by $\rho_i=m_id_i$. In the SDPD formulation for Newtonian fluids, the stress tensor $\Pi_i=p_i^s\mathbf{1}$ contains only diagonal (i.e., pressure) components. The pressure p_i^s is determined by the equation of state (EoS) $p_i^s=p_0(d_i/d_0)^\nu-p_b$, where d_0 is the average number density, and p_0 , ν , and p_b are freely selected parameters. Furthermore, γ_{ij} and σ_{ij} are the corresponding force amplitudes defined as

$$\gamma_{ij} = \frac{20\eta}{7} \frac{F_{ij}}{d_i d_i}, \quad \sigma_{ij} = 2\sqrt{k_{\rm B} T \gamma_{ij}}, \tag{2}$$

where η is the fluid dynamic viscosity and T is the equilibrium temperature. Equation (1) also contains a matrix of independent Wiener increments dW_{ij} with its trace $\operatorname{tr}[dW_{ij}]$ and the traceless symmetric part $d\bar{W}_{ij}^s = \frac{1}{2}(dW_{ij} + dW_{ji}) - \frac{1}{3}\operatorname{tr}[dW_{ij}]$, and the time step Δt .

The evolution of particle positions, translational, and angular velocities is obtained by integration of the following equations of motion:

$$\dot{\mathbf{r}}_{i} = \mathbf{v}_{i},
m_{i}\dot{\mathbf{v}}_{i} = \sum_{j} \mathbf{F}_{ij} = \sum_{j} (\mathbf{F}_{ij}^{C} + \mathbf{F}_{ij}^{D} + \mathbf{F}_{ij}^{R} + \tilde{\mathbf{F}}_{ij}),
\dot{\boldsymbol{\psi}}_{i} = \frac{1}{2I_{i}} \sum_{i} \mathbf{r}_{ij} \times \mathbf{F}_{ij},$$
(3)

using the velocity-Verlet algorithm.43

Fluid elasticity is introduced following the idea that every fluid particle contains $N_{\rm p}$ bead-spring dumbbells.³⁷ Dumbbells are not explicitly modeled, but represented by a conformation tensor c that characterizes their stretching state within each particle. The conformation tensor is expressed as $c_i = 1/N_{\rm p} \sum_a^{N_{\rm p}} q_a q_a$, where q_a is the end-to-end distance of the a-th dumbbell within a fluid particle i. Then, the stress tensor Π_i in Eq. (1) is modified by the addition of c contribution as follows:³⁷

$$\mathbf{\Pi}_i = p_i^{\mathrm{s}} \mathbf{I} + \mathbf{N}_{\mathrm{p}} \mathbf{d}_{\mathrm{i}} \mathbf{k}_{\mathrm{B}} \mathbf{T} (\mathbf{I} - \mathbf{c}_{\mathrm{i}}). \tag{4}$$

Evolution of the conformation tensor proceeds according to 37

$$\dot{\boldsymbol{c}}_{i}^{\mu\mu'} = \frac{1}{d_{i}} \boldsymbol{c}_{i}^{\mu\nu} \boldsymbol{\kappa}_{i}^{\nu\mu'} + \frac{1}{d_{i}} \boldsymbol{c}_{i}^{\mu'\nu} \boldsymbol{\kappa}_{i}^{\nu\mu} + \frac{1}{\tau} (\delta^{\mu\mu'} - \boldsymbol{c}_{i}^{\mu\mu'}) + \frac{d\tilde{\boldsymbol{c}}_{i}^{\mu\mu'}}{\Delta t}, \quad (5)$$

where $\kappa_i^{\mu\nu}=\sum_j F_{ij} r_{ij}^\mu v_{ij}^\nu$ is the velocity gradient tensor, τ is the dumb-bell relaxation time, and $d\tilde{c}$ is the noise term. This model corresponds to the well-known viscoelastic Oldroyd-B model, in which the total fluid viscosity $\eta=\eta_{\rm s}+\eta_{\rm p}$ has two contributions, including solvent $\eta_{\rm s}$ and polymer $\eta_{\rm p}$ components. The polymer contribution is given by $\eta_{\rm p}=k_{\rm B}Td_0N_{\rm p}\tau$ and can easily be adjusted through the parameters $N_{\rm p}$ and τ .

In this work, the smoothing kernel is represented by the two dimensional (2D) Lucy function⁴⁴

$$W(r) = \frac{5}{\pi r_c^2} \left(1 + 3 \frac{r}{r_c} \right) \left(1 - \frac{r}{r_c} \right)^3.$$
 (6)

Thermal fluctuations are neglected by setting $k_{\rm B}T=10^{-6}$, such that the SDPD method is essentially reduced to SPH. Furthermore, we also neglect the noise term of the conformation tensor, i.e., $d\tilde{c}=0$.

B. Sheet model and simulation setup

Figure 1(a) shows a schematic of our 2D simulation setup with two sheets. According to the theoretical work of Taylor, ¹⁷ traveling wave $y(x,t)=b\sin(kx-\omega t+\phi)$ of an inextensible 2D sheet can be modeled through the imposition of particle velocities as

$$v_x = \frac{\omega}{k} - Q\cos\theta, \quad v_y = -Q\sin\theta,$$

$$\tan\theta = bk\cos(kx - \omega t + \phi),$$

$$Q = \frac{\omega}{2\pi k} \int_0^{2\pi} \left(1 + b^2 k^2 \cos^2 \xi\right)^{1/2} d\xi,$$
(7)

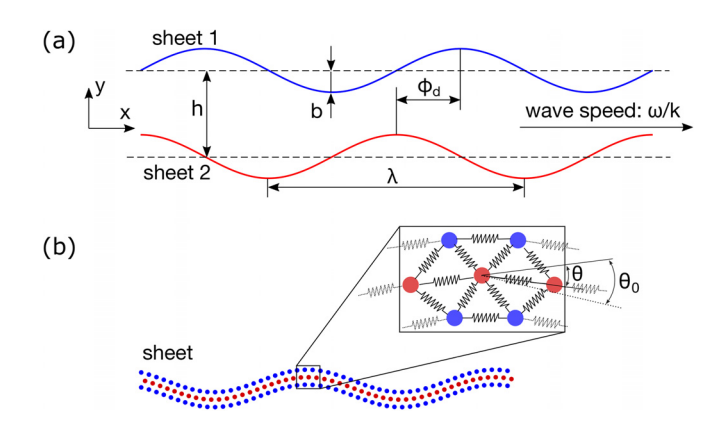


FIG. 1. Model schematic. (a) Setup and basic parameters of the two actuated sheets. Here, b is the wave amplitude, k is the wave number, $\lambda = 2\pi/k$ is the wavelength, ω is the wave frequency, such that the wave speed is ω/k . h is the distance between average positions of the sheets and $\phi_{\rm d}$ is a phase difference between their actuations. (b) Model representation of a flexible sheet constructed by three particle layers interconnected by springs. θ is the instantaneous angle between two adjacent springs in the middle layer (marked in red), and θ_0 is the spontaneous angle employed for sheet actuation.

where b is the wave amplitude, k is the wave number related to the wavelength $\lambda=2\pi/k$, ω is the wave angular frequency, and ϕ is the phase shift. Even though this traveling wave propagates with a wave speed ω/k , material points of the sheet do not move forward or backward on average, and thus they represent a waving (rather than swimming) sheet, which will be referred to as *prescribed actuation* further in text. However, such sheet actuation generates a far-field flow, ¹⁷ which can result in non-zero hydrodynamic synchronization forces between the two waving sheets.

The prescribed actuation strategy in Eq. (7) cannot be used to model dynamic synchronization of two swimming sheets. Furthermore, it does not account for a possible flexural rigidity of the sheets. Model of a flexible sheet is shown in Fig. 1(b), where three layers of sheet particles are interconnected by harmonic springs. The spring potential is given by

$$U(l) = \frac{\zeta_{\rm s}}{2} (l - l_0)^2, \tag{8}$$

where ζ_s is the spring stiffness, l is its length, and l_0 is the equilibrium spring length. Actuation of the flexible sheets is performed using the middle layer [marked red in Fig. 1(b)], where a harmonic angle potential

$$U(\theta) = \frac{\zeta_{\theta}}{2} (\theta - \theta_0)^2 \tag{9}$$

is implemented for each pair of adjacent springs. Here, ζ_{θ} is the potential strength, θ is the instantaneous angle between two adjacent springs in the middle layer, and θ_0 is the spontaneous angle. A traveling wave on the sheets is imposed by varying $\theta_0(x,t)=\theta_b\sin{(kx_s-\omega t)}$, where θ_b is the angle amplitude and $x_s=il_0$ is the distance along the sheet with i representing particle numbering along the middle layer. Flexural rigidity κ of this model can be estimated as $\kappa=2\zeta_s l_0^3+\zeta_\theta l_0$ (see the Appendix). In addition to the parameters ζ_θ and θ_b , the actual wave amplitude in this case is

affected by the sheet flexural rigidity, wave frequency, and fluid viscoelasticity. This model of sheet motion will be referred to as *internal actuation* and allows the simulation of dynamic synchronization of two swimming sheets.

In simulations, the two sheets separated by a distance h between their average positions are embedded into the modeled SDPD fluid. Each sheet is constructed by three layers of particles and is driven either through the prescribed actuation [see Eq. (7)] or by internal actuation [see Eq. (9)]. The number density of sheet particles is the same as that of fluid particles. Therefore, interactions between fluid and sheet particles are identical to the fluid-fluid interactions. The simulation domain $L_x \times L_y$ is periodic in both dimensions. Note that the periodicity in y direction leads to the fact that the simulation system represents infinitely many sheets. However, we have verified for several parameter sets that L_y is large enough to have a negligible effect on synchronization results, and therefore, this periodic system is a good approximation for two sheets in an infinite domain.

Basic simulation parameters are summarized in Table I. For the reproducibility of simulation results, all simulation parameters are explicitly specified in terms of the cutoff radius $r_c=1.6$, reference mass density $\rho_{\rm ref}=6.25$, and dynamic viscosity $\eta_{\rm ref}=20$, which also define a reference pressure $p_{\rm ref}=\eta_{\rm ref}^2/(r_c^2\rho_{\rm ref})$ and flexural rigidity $\kappa_{\rm ref}=\eta_{\rm ref}^2/r_c/\rho_{\rm ref}$. Nevertheless, all simulation results are presented in terms of relevant physical scales, such as a length scale 1/k and a timescale $1/\omega$, or several non-dimensional groups defined later.

C. Model validation

Since our SDPD formulation is practically reduced to SPH by neglecting random terms, we can take advantage of rich SPH literature for the method validation. For instance, a similar SPH formulation has been used to simulate different fluid flows at low and moderate Re, 46,47 in good agreement with the corresponding analytical and/or finite-element results. Note that SPH may become unstable at high Re. 48 To verify the correctness of SDPD implementation for Newtonian fluids, wall-bounded Poiseuille flow and unsteady flow above an oscillating plate (or Stokes second problem) were simulated, showing an excellent agreement with the corresponding analytical solutions. The viscoelastic Oldroyd-B model has also been validated using unsteady Kolmogorov flow. 37

In the context of swimming sheets, we revisit the problem of a single waving sheet both in Newtonian and in viscoelastic fluids. An inextensible 2D sheet actuated according to Eq. (7) generates a far-field flow velocity $V_{\rm N}$ in the x direction. The theoretical prediction of $V_{\rm N}$ is given by 17

$$V_{\rm N} = \frac{1}{2}\omega b^2 k \left(1 - \frac{19}{16}b^2 k^2 \right). \tag{10}$$

Figure 2(a) compares simulation results for $V_{\rm N}$ in a Newtonian fluid to the theoretical prediction in Eq. (10), demonstrating an excellent agreement. Here, Re \in [2.8 \times 10⁻⁴, 5.6 \times 10⁻³], defined as Re $= \omega b^2 \rho/\eta$, remains small for all simulations in Fig. 2(a). The theoretical result by Tuck²² for Re > 0 is also shown in Fig. 2(a); however, it is only of the order $\mathcal{O}(b^2k^2)$ and is therefore less accurate.

For viscoelastic Oldroyd-B fluids, a theoretical prediction for the far-field velocity $V_{\rm ve}$ generated by a waving sheet is given by 45

TABLE I. Basic parameters used in simulations. The reference units are introduced for the non-dimensionalization of all simulation parameters, so that the performed simulations can easily be reproduced. The reference values represent parameter magnitudes most frequently used in simulations.

Basic parameters	Values (model units)
Cutoff radius r_c	1.6
Reference mass density $ ho_{ m ref}$	6.25
Reference dynamic viscosity $\eta_{\rm ref}$	20
Energy unit $k_B T$	10^{-6}
Size of the simulation domain $L_x \times L_y$	$12.5r_c \times 18.75r_c$
Wave number <i>k</i>	$4\pi/L_x$
Average number density d_0	$16/r_c^2$
Average distance between the two sheets <i>h</i>	$2.875r_{c}$
Angle potential strength ζ_{θ}	$62.5\eta_{\rm ref}^2/\rho_{\rm ref}$
Hydrostatic pressure $p_0 - p_b$	$3.2\eta_{\rm ref}^2/(r_c^2\rho_{\rm ref})$
Exponent in the EoS $ u$	7

$$V_{\rm ve} = \frac{1}{2}\omega b^2 k \frac{1 + {\rm De}^2 \eta_{\rm s}/\eta}{1 + {\rm De}^2},\tag{11}$$

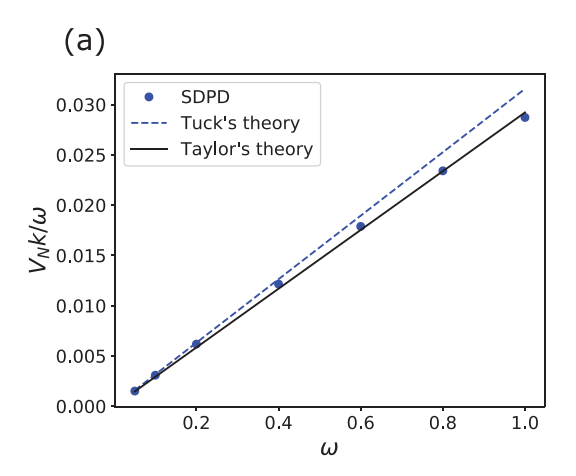
where η_s is the solvent component of viscosity and $De = \tau \omega$ is the Deborah number that represents a ratio of relaxation time to the characteristic time of sheet motion. Figure 2(b) shows the comparison of simulated V_{ve} for a waving sheet in various viscoelastic fluids against the analytical prediction in Eq. (11) as a function of De. The simulation results (symbols) for various η_s/η agree well with the analytical prediction (solid line). The theoretical result for an infinite domain in Eq. (11) has also been extended toward sheet swimming in an Oldroyd-B fluid next to a boundary.

III. RESULTS AND DISCUSSION

We investigate the synchronization of two sheets, and in particular, its dependence on inertial effects, fluid compressibility, sheet flexural rigidity, and fluid viscoelastic properties. Two sheets placed side by side with a distance h apart (see Fig. 1) can have a phase difference in their motion given by $\phi_{\rm d}=\phi_2-\phi_1$. Generally, the synchronization force in the x direction is a function of $\phi_{\rm d}$ and can be approximated by a functional form motivated by theoretical predictions for low amplitudes 30,31

$$F^{s}(\phi_{d}) = \bar{F}^{s} \sin{(\phi_{d})}, \tag{12}$$

where \bar{F}^s is the force amplitude. The synchronization forces on the two sheets have the same magnitude, but different signs, which means that they act in opposite directions. For the calculation of force amplitude \bar{F}^s , several simulations for different $\phi_{\rm d}$ values in the interval $[0,\pi]$ (with an increment of $\pi/30$ for simulations with Newtonian fluids and of $\pi/15$ for simulations with Oldroyd-B fluids) are performed, and the resultant force data are fitted using Eq. (12). Note that the force amplitude \bar{F}^s can also be negative, as the fitting is carried out within the range $[0,\pi]$. For $bk \lesssim 0.5$, the sine function in Eq. (12) is an accurate representation of $F^s(\phi_{\rm d})$. For bk > 0.5, even though synchronization force profiles start departing from the sine form, fitting $F^s(\phi_{\rm d})$ with the sine function still provides a good approximation of the force amplitude \bar{F}^s .



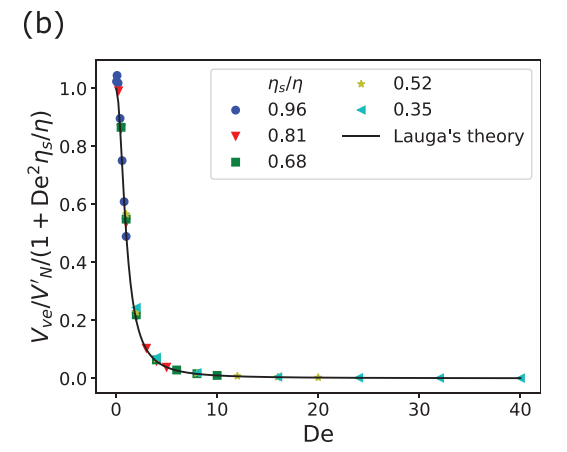


FIG. 2. Model validation. (a) Far-field velocity V_N generated by a single waving sheet in a Newtonian fluid in comparison with the theoretical prediction by Taylor¹⁷ for Re = 0 [Eq. (10)] and by Tuck²² for Re > 0. Here, $\eta/\eta_{\rm ref} = 20$. (b) Comparison of simulated and theoretical far-field velocities $V_{\rm ve}$ generated by a waving sheet in viscoelastic fluids for various $\eta_{\rm s}/\eta$. The theoretical prediction corresponds to Eq. (11).⁴⁵ The simulation results collapse onto a single curve when $V_{\rm ve}$ is normalized by $V_{\rm N}'(1 + {\rm De}^2\eta_{\rm s}/\eta)$, where $V_{\rm N}' = \omega b^2 k/2$ is the first term of the Taylor's prediction. Here, $N_{\rm p} = 3 \times 10^6$ and $\eta_{\rm s}/\eta_{\rm ref} = 20$ are fixed. In all simulations, $L_{\rm x} \times L_{\rm y} = 18.75 r_{\rm c} \times 31.25 r_{\rm c}$, bk = 0.25, and $p_0/p_{\rm ref} = 40$.

There exist two possible synchronized configurations:

- (i) $\phi_{\rm d}=0$ —an in-phase configuration,
- (ii) $\phi_d = \pi$ —an opposite-phase configuration.

Due to the choice of initial sheet positions with a phase difference $0 \le \phi_{\rm d} = \phi_2 - \phi_1 \le \pi$ in Fig. 1, the synchronization forces $F_1^s(\phi_{\rm d}) = -F_2^s(\phi_{\rm d}) < 0$ drive the sheets toward the in-phase configuration with $\phi_{\rm d} = 0$, while for $F_1^s(\phi_{\rm d}) = -F_2^s(\phi_{\rm d}) > 0$, the opposite-phase conformation with $\phi_{\rm d} = \pi$ is stable. Further, simulation results will mainly be presented in terms of \bar{F}_1^s for the first sheet only.

A. Synchronization in Newtonian fluids

1. Interaction of two waving sheets

Figure 3 presents synchronization force amplitudes of the first waving sheet with prescribed actuation as a function of $t_s/t_d = \eta/(b\rho c)$ for different values of sound speed $c = \sqrt{p_0 \nu / \rho}$. Here, t_s/t_d characterizes the interplay between inertial and fluid-compressibility effects for synchronization, where $t_s = b/c$ corresponds to a timescale of pressure (sound) wave and $t_d = b^2 \rho / \eta$ represents a viscous diffusion timescale for momentum transfer. Despite the fact that the viscous diffusion timescale is relevant here, symmetry breaking for the synchronization of two sheets in an incompressible fluid is provided by the inertial term in Navier–Stokes equations, as at Re = 0, no synchronization should occur.²⁵ Therefore, the word "effect" will always refer to the relevant symmetry breaking mechanism. For instance, the expression "inertial effects" represents symmetry breaking due to a non-negligible inertia, even though the synchronization proceeds due to viscous forces. For $t_s/t_d \gtrsim 0.5$, synchronization forces in Fig. 3 favor the in-phase configuration when the momentum transfer by compressional wave dynamics due to fluid compressibility dominates. For $t_s/t_d \lesssim 0.5$, fluid compressibility effects can be neglected, and the opposite-phase synchronization is mediated by viscous forces due to inertial effects. Note that in the case of $t_s/t_d \ll 1$ or when inertial effects dominate, \bar{F}_1^s is nearly independent of t_s/t_d (and also η) as shown in the inset of Fig. 3.

In the limit of incompressible fluid at Re = 0, no synchronization (i.e., $\bar{F}_s^i = 0$) should occur for two interacting sheets having a reflection symmetry with respect to the y axis, show the imposed sine wave here. Our simulation results in Fig. 3 show relatively small but not vanishing synchronization forces for Re \in [0.04, 1] and $t_s/t_d < 0.1$. These arguments suggest that for an incompressible fluid, inertial effects (i.e., Re > 0) should lead to the stable opposite-phase configuration with $\bar{F}_s^i > 0$ that vanishes at Re = 0. For comparison, human sperm typically has a beating frequency of $f \approx 20$ Hz and an amplitude of $b \approx 10 \ \mu m$, show the stable opposite in the stable opposit

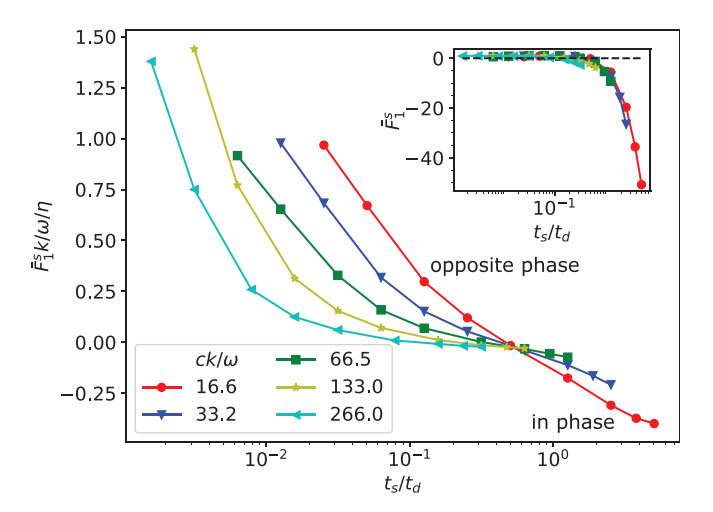


FIG. 3. Synchronization force amplitudes \bar{F}_1^s of the first waving sheet with prescribed actuation as a function of $t_s/t_d=\eta/(b\rho c)$ for different sound speeds $c=\sqrt{p_0\nu/\rho}$ in a Newtonian fluid. Both η and p_0 are varied such that $\eta/\eta_{\rm ref}\in[0.05,10]$ and $p_0/p_{\rm ref}\in[4,1024]$. Note that $\bar{F}_2^s=-\bar{F}_3^s$. In all cases, $\omega=0.4$ and bk=0.25. Inset shows that dimensional values of \bar{F}_1^s fall onto a single curve as a function of t_s/t_d .

Re ≈ 0.01 and $t_s/t_d \approx 7 \times 10^{-5}$ in a water-like environment. For existing microrobots, typical non-dimensional numbers are Re $\sim \mathcal{O}(1)$ and $t_s/t_d \sim \mathcal{O}(10^{-3})$. Thus, inertial effects are expected to be pertinent for all microswimmers, while fluid compressibility can become relevant to swimming in highly viscous fluids. For instance, the viscosity of human mucus at low shear rates can be 10^4-10^6 times larger than that of water, 53 leading to t_s/t_d values on the order of $\mathcal{O}(1)$.

To systematically investigate the synchronization of inextensible sheets, different parameters (other than η) are varied. Figure 4 shows synchronization force amplitudes of the first waving sheet (prescribed actuation) as a function of wave frequency ω , wave amplitude b, and fluid mass density ρ . In Fig. 4(a), $t_s/t_d=0.063$ is independent of ω , and \bar{F}_1^s nearly vanishes at small ω or Re values. Figures 4(b) and 4(c) show that depending on t_s/t_d , the opposite-phase configuration due to inertial effects or the in-phase configuration due to fluid-compressibility effects takes place, which is consistent with the results in Fig. 3. When inertial effects dominate at $t_s/t_d \lesssim 0.5$, the opposite-phase conformation takes place, and the magnitude of \bar{F}_1^s increases significantly with increasing ω , b, and ρ . Insets in Fig. 4 show that at large enough values of these parameters, the synchronization force

amplitude \bar{F}_1^s exhibits a power-law dependence with respect to the wave frequency ω , wave amplitude b, and fluid mass density ρ . Remember that \bar{F}_1^s is nearly independent of fluid viscosity η , when fluid compressibility effects can be neglected, see the inset of Fig. 3. Therefore, the results in Figs. 3 and 4 indicate that dimensionless synchronization forces in the regime of inertial effects are proportional to Re as

$$\frac{\bar{F}_1^s k}{n\omega} \propto \text{Re}.$$
 (13)

This equation remains valid even for relatively large bk values, as the relation $\bar{F}_1^s \propto b^2$ holds up to bk = 0.75 in Fig. 5. As we will show later, an increase in the synchronization force amplitude for large bk can be much faster than b^2 for viscoelastic fluids.

2. Dynamic synchronization of two flexible sheets

To investigate dynamic synchronization process of two beating sheets, we employ the setup with two flexible sheets that have internal actuation. To characterize synchronization dynamics, synchronization

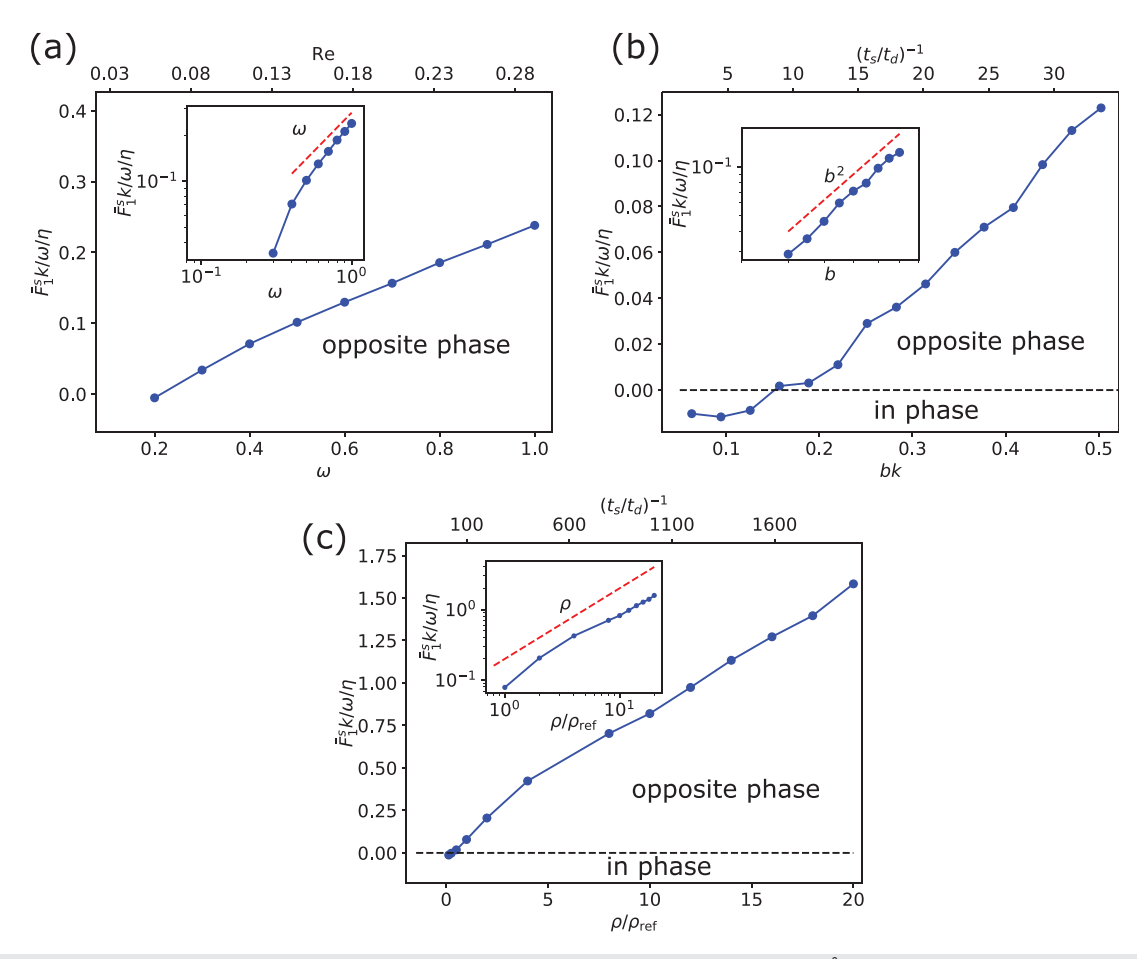


FIG. 4. Synchronization force amplitudes of the first waving sheet (prescribed actuation) for various parameters. (a) \bar{F}_1^s as a function of wave frequency ω with bk=0.25. Here, $t_s/t_d=0.063$. (b) \bar{F}_1^s as a function of wave amplitude b with $\omega=0.4$. (c) \bar{F}_1^s as a function of fluid mass density ρ . Here, $\omega=0.4$ and bk=0.25. Other parameters, such as $\eta/\eta_{\rm ref}=1$ and $p_0/p_{\rm ref}=256$, are fixed in all simulations. Insets show absolute values of \bar{F}_1^s in log-log plots.

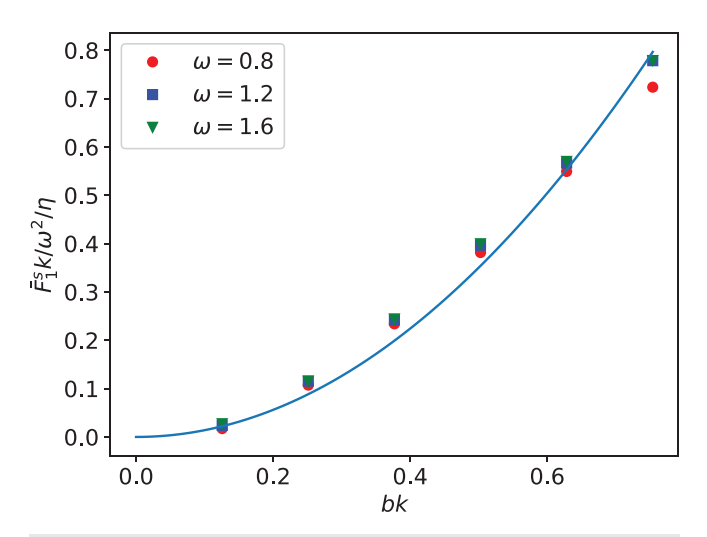


FIG. 5. Synchronization force amplitudes with non-negligible inertia as a function of bk. Here, the non-dimensional force $\bar{F}_1^s k/(\eta \omega)$ is divided by ω so that all data collapse onto a single curve, as $\bar{F}_1^s \propto \omega^2$. The solid line represents a fit with quadratic function. $\eta/\eta_{\rm ref}=1$ and $p_0/p_{\rm ref}=256$ are used in simulations.

time τ^s is first introduced. Since our simulations demonstrate that for $bk \lesssim 0.5$, the synchronization forces F_1^s and F_2^s have a sine-function dependence on ϕ_d [see Eq. (12)], independently of the contributing factors, such as fluid compressibility, inertial effects, and sheet flexibility, the dynamic synchronization process can be described as a damped harmonic oscillator

$$\frac{d^2\phi_{\rm d}}{dt^2} = -a_1 \frac{d\phi_{\rm d}}{dt} - a_2 \sin{(\phi_{\rm d})}.$$
 (14)

Here, a_1 is a characteristic frequency and a_2 is related to the synchronization force amplitudes \bar{F}_1^s and \bar{F}_2^s , which are either negative or positive, depending on whether the in-phase or opposite-phase configuration is stable. Note that the functional form of \bar{F}_2^s and \bar{F}_2^s

departs from the sine function at large bk > 0.5, but Eq. (14) still remains a reasonable approximation for dynamic synchronization.

In general, a_1 can be a function of $\phi_{\rm d}$, but for simplicity, it is assumed to be constant here. A process described by Eq. (14) can have an oscillating dynamics, if the inertial term represented by the second time derivative is large enough. Our simulations (not presented here) have shown that an oscillation in the synchronization of two flexible sheets may occur at high Re. However, in all cases studied here, Re is small enough so that the synchronization process of two sheets can be considered overdamped, even though it may be caused by inertial effects. By neglecting the inertial term in Eq. (14), an Adler-like equation 54 $d\phi_{\rm d}/dt = -a_2/a_1\sin{(\phi_{\rm d})}$ for $\phi_{\rm d}$ is obtained, which has an analytical solution given by 55

$$\phi_{\rm d} = 2 \tan^{-1} \left(\tan \frac{\phi_{\rm d}^0}{2} e^{-a_2 t/a_1} \right),$$
 (15)

where $\phi_{\rm d}^0$ is the initial phase difference at time t=0. Equation (15) is used to extract the synchronization time as $\tau^s=|a_1/a_2|$ from simulations of dynamic synchronization. Figures 6(a) and 7(a) show such fits by dashed lines and demonstrate that they approximate well time-dependent simulation data. Furthermore, the physical meaning and dimensions of a_1 and a_2 suggest that $a_1 \propto \omega$ and $a_2 \propto \omega^2 \bar{F}^s k/(\eta \omega)$, resulting in

$$\tau^{\rm s} \propto \frac{\eta}{\bar{F}^{\rm s} k}.$$
(16)

Figure 6(a) shows time-dependent phase difference ϕ_d between two flexible sheets for various t_s/t_d (η is varied). At low enough t_s/t_d , the sheets attain the opposite-phase configuration because of inertial effects. As t_s/t_d is increased, the in-phase configuration becomes stable due to the combined effect of fluid compressibility mentioned above and sheet flexibility that will be discussed below. Note that in the case of internal actuation the wave amplitude b of flexible sheets is reduced significantly by increasing η [see Fig. 6(b)] because of an increased viscous resistance on the sheets. Nevertheless, the behavior of τ^s in Fig. 6(a) is non-monotonic with t_s/t_d (or with η) due to several reasons. In

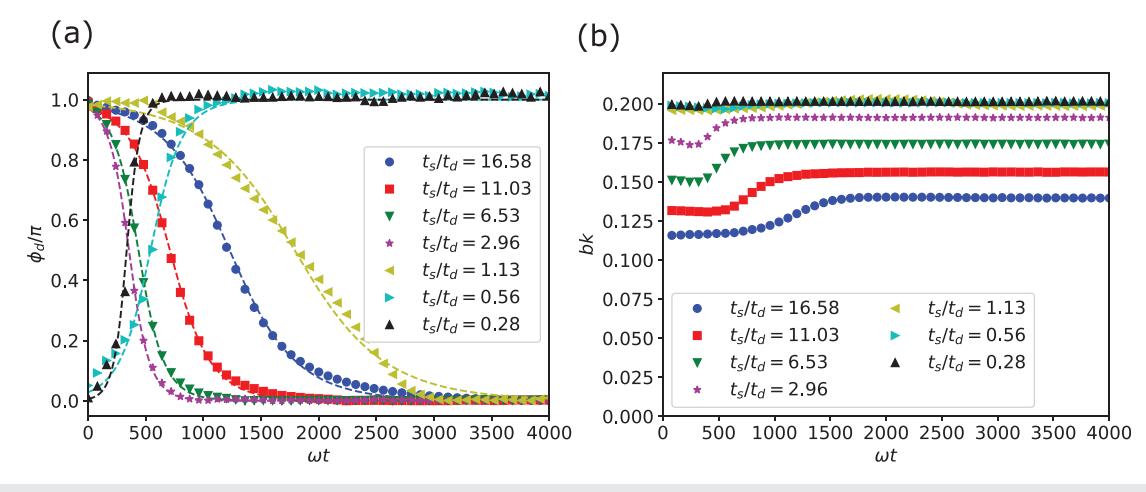


FIG. 6. Dynamic synchronization of two flexible sheets (internal actuation) for different t_s/t_d (η is varied). (a) Phase difference plotted by symbols as a function of time. The dashed lines correspond to data fitting using Eq. (15). (b) Beating wave amplitude b for various t_s/t_d . Here, $\omega=1.0$, $\theta_b/\pi=0.028$, $\kappa/\kappa_{\text{ref}}=28.125$, $\rho_0/\rho_{\text{ref}}=4$, and $\nu=5$.

the case of stable opposite-phase configuration $(t_s/t_d \le 1 \text{ here})$, where fluid inertial effects dominate, τ^s increases with increasing t_s/t_d (also with increasing η) because the synchronization force amplitude \bar{F}^s is independent of η [see the inset of Fig. 3] and the synchronization time is proportional to η/\bar{F}^s [see Eq. (16)]. The case of $t_s/t_d = 1.13$ exhibits the largest τ^s , since it is near the opposite-phase to in-phase transition, at which the synchronization force vanishes. With a further increase in t_s/t_d , the synchronization time first decreases due to an increase in the synchronization forces, but then increases for $t_s/t_d \ge 2.96$ due to the decreasing beating amplitude shown in Fig. 6(b).

To directly demonstrate the effect of sheet flexibility, Fig. 7(a) shows the transition from opposite-phase to in-phase configuration for different $\alpha = \pi^4 \rho b \omega^2 / (\kappa k^4)$, which represents the ratio of viscous stresses $\sim \rho b^2 \omega^2$ (see Fig. 4) and bending stresses $\sim \kappa b/(\lambda/2)^4$ $= \kappa b k^4/\pi^4$ (flexural rigidity κ is varied through the spring stiffness ζ_s). Here, fluid compressibility effects can be neglected as $t_s/t_d \approx 0.05$. Interestingly, stiff sheets (i.e., small α) synchronize toward the opposite-phase configuration due to inertial effects, while soft sheets are driven toward the in-phase conformation, even though the effective Re increases with increasing α due to an increase in wave amplitude, see Fig. 7(b). Therefore, sheet flexibility drives the system of two sheets toward the in-phase configuration for $\alpha \ge 1$. This result is consistent with the theory predicting that a finite elasticity of two sheets in an incompressible fluid is sufficient to break the symmetry and exhibit the in-phase synchronization at Re = 0.30 Furthermore, a simulation study²⁸ of a pair of flexible sheets based on the incompressible Navier-Stokes equations reports the transition from in-phase to opposite-phase conformation with increasing Re, in agreement with the discussed results.

Considering $\bar{F}_1^s k/(\omega \eta) \propto \text{Re}$ that has been hypothesized in Eq. (13) for two waving sheets, the synchronization time τ^s normalized by the wave frequency ω simply becomes

$$\tau^{s}\omega \propto \frac{1}{\text{Re}}.$$
(17)

This relation is tested by a number of simulations for various ω , ρ , η , and θ_b values. Figure 8(a) shows τ^s for $\kappa/\kappa_{\rm ref} = 20.63$ and $p_0/p_{\rm ref}$

= 256 as a function of Re. When inertial effects dominate at large enough Re, τ^s is inversely proportional to Re, as predicted. At low Re, where t_s/t_d and α increase, the effects of fluid compressibility and sheet flexibility become important, so that τ^s deviates from the relation in Eq. (17). Figure 8(b) presents simulation data for $\kappa/\kappa_{\rm ref}=35.63$ and $p_0/p_{\rm ref}=1024$, such that both fluid compressibility and sheet flexibility effects are significantly reduced. The behavior of τ^s closely follows the relation in Eq. (17) for a wide range of Re numbers. Noteworthy, the rapid increase in τ^s at small Re in Fig. 8 is qualitatively consistent with the theoretical prediction that no synchronization of two inextensible sheets having a reflection symmetry with respect to the y axis can occur at Re = 0.45

B. Synchronization in viscoelastic fluids

Fluid elasticity is also sufficient to break the symmetry and result in the in-phase synchronization of two inextensible sheets at Re = 0. Theoretical prediction for the synchronization force between two sheets up to the order $\mathcal{O}(b^2k^2)$ is given by 31

$$\frac{F_{1}^{s}(\phi_{d})k}{\omega\eta} = \left[\frac{2\pi\Delta U}{kh} - \frac{4\pi \text{De}\eta_{p}}{\eta(1 + \text{De}^{2})}A(kh)\sin(\phi_{d})\right](bk)^{2},$$

$$A(kh) = \frac{kh\cosh(kh) + \sinh(kh)}{\cosh(2kh) - 2k^{2}h^{2} - 1},$$
(18)

where ΔU is the relative velocity of two sheets and $\eta = \eta_{\rm p} + \eta_{\rm s}$ includes polymer and solvent viscosity contributions. In the case of two waving sheets with prescribed actuation, $\Delta U = 0$. Note that for $\Delta U = 0$, the synchronization force in Eq. (18) can be written as $F_1^s(\phi_{\rm d}) = \bar{F}_1^s \sin{(\phi_{\rm d})}$, which is identical to Eq. (12) hypothesized before.

Figure 9(a) presents the non-dimensional force $\bar{F}_1^s k/(\omega \eta)$ obtained from a number of simulations (symbols) of two waving sheets in viscoelastic fluids with respect to the theoretical prediction (solid lines) in Eq. (18) for several bk values. An excellent agreement between simulated and theoretical synchronization force amplitudes is achieved. In these simulations, the wave frequency $\omega \in [0.4, 1.6]$,

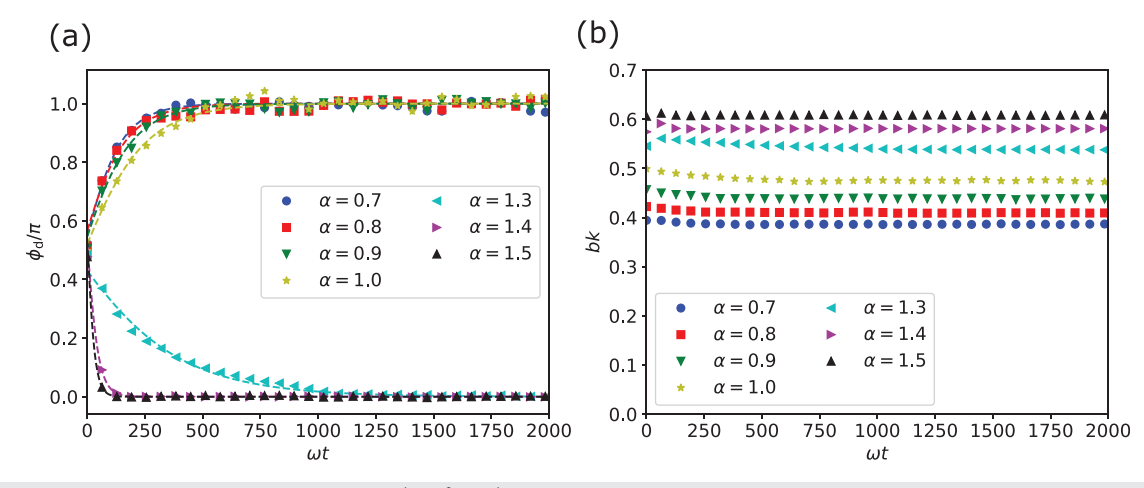


FIG. 7. Synchronization of two flexible sheets for various $\alpha=\pi^4\rho b\omega^2/(\kappa k^4)$ that characterizes competition between viscous and bending stresses. (a) Phase difference $\phi_{\rm d}$. Simulated data are shown by symbols, while the dashed lines represent fits using Eq. (15). (b) Wave amplitude b. Here, $\kappa/\kappa_{\rm ref}\in[15.86,20.63],~\omega=0.8,~\eta/\eta_{\rm ref}=1,~\theta_b/\pi=0.044,~{\rm and}~p_0/p_{\rm ref}=256.$

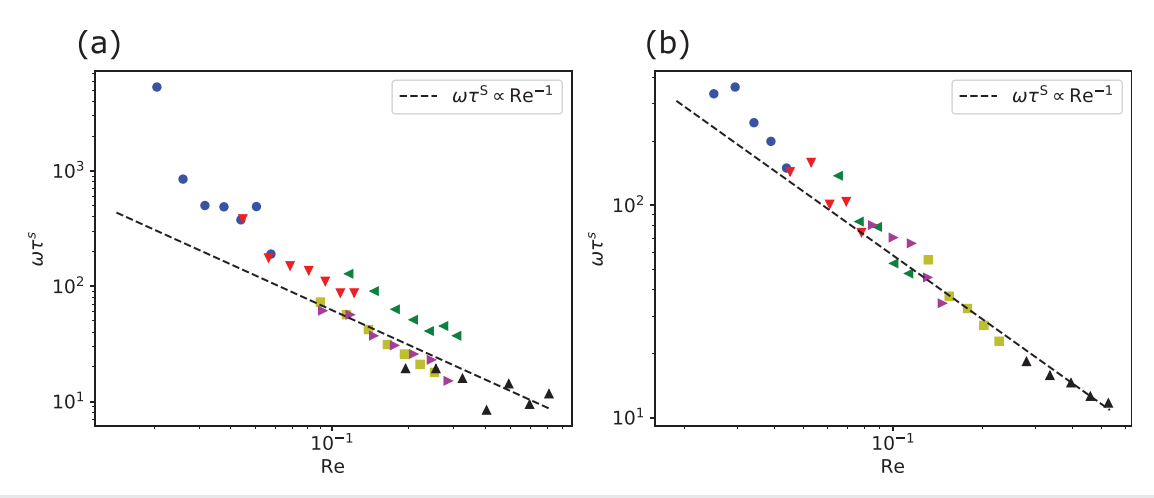


FIG. 8. Dependence of synchronization time τ^s on ω and Re. (a) Simulations with $\kappa/\kappa_{\rm ref}=20.63$ and $\rho_0/\rho_{\rm ref}=256$. Different datasets are plotted by symbols, corresponding to $\theta_b/\pi=0.028$ (blue circles); $\theta_b/\pi=0.044$ (red down-pointing triangles); $\theta_b/\pi=0.089$ (green left-pointing triangles); $\eta/\eta_{\rm ref}=0.5$ and $\theta_b/\pi=0.044$ (yellow squares); $\rho/\rho_{\rm ref}=2$ and $\theta_b/\pi=0.044$ (purple right-pointing triangles); and $\rho/\rho_{\rm ref}=4$ and $\theta_b/\pi=0.044$ (black up-pointing triangles). (b) Simulations with $\kappa/\kappa_{\rm ref}=35.63$ and $\rho_0/\rho_{\rm ref}=1024$. Various symbols represent $\theta_b/\pi=0.044$ (blue circles); $\theta_b/\pi=0.067$ (red down-pointing triangles); $\theta_b/\pi=0.089$ (green left-pointing triangles); $\eta/\eta_{\rm ref}=0.5$ and $\theta_b/\pi=0.089$ (yellow squares); $\theta_b/\pi=0.11$ (purple right-pointing triangles); $\rho/\rho_{\rm ref}=4$ and $\theta_b/\pi=0.089$ (black up-pointing triangles). Each set of data includes several ω values in the range [0.2, 1.0]. If not explicitly specified, $\eta/\eta_{\rm ref}=1$ are used in simulations. The dashed lines indicate Re⁻¹.

wave amplitude bk, and relaxation time τ are varied, while the viscosities $\eta_s/\eta=0.1875$ and $\eta_s/\eta_{\rm ref}=0.9375$ are kept constant. Note that the values of $N_{\rm p}$ and τ are adjusted to keep $\eta_{\rm p}=k_{\rm B}Td_0N_{\rm p}\tau$ fixed. In all simulations, $t_s/t_d\gg 0.1$ to minimize inertial effects. Fluid compressibility effects can also be neglected, because the ratio $t_s/\tau=b/(c\tau)$, which compares compressibility and viscoelasticity effects, is much smaller than unity for all τ values used in simulations.

Figure 9(b) demonstrates that the simulated force amplitudes scaled as $\bar{F}_1^s/(\omega\eta b^2 k)$ fall onto a single master curve that is well captured by the theoretical prediction in Eq. (18). Furthermore, Fig. 9 shows that the maximum synchronization force is achieved at De = 1 for a fixed bk and ω . Noteworthy, for a fixed ω , the synchronization

force amplitude asymptotically approaches zero with increasing De or τ . This indicates that the synchronization of flagellated microswimmers must be weak in viscoelastic fluids with a large relaxation time. In fact, De for realistic biological microswimmers can be significantly larger than unity. For instance, De is between 10^2 and 10^3 for the case of sperm cells swimming in mucus, whose relaxation time is in the range of 1-10 s. ³¹

Figure 10(a) presents dynamic synchronization of two flexible sheets for various De, and demonstrates that this process is fastest at De=1, in agreement with the theoretical prediction in Eq. (18). The corresponding beating wave amplitudes shown in Fig. 10(b) are small enough in these simulations, such that the theoretical prediction is

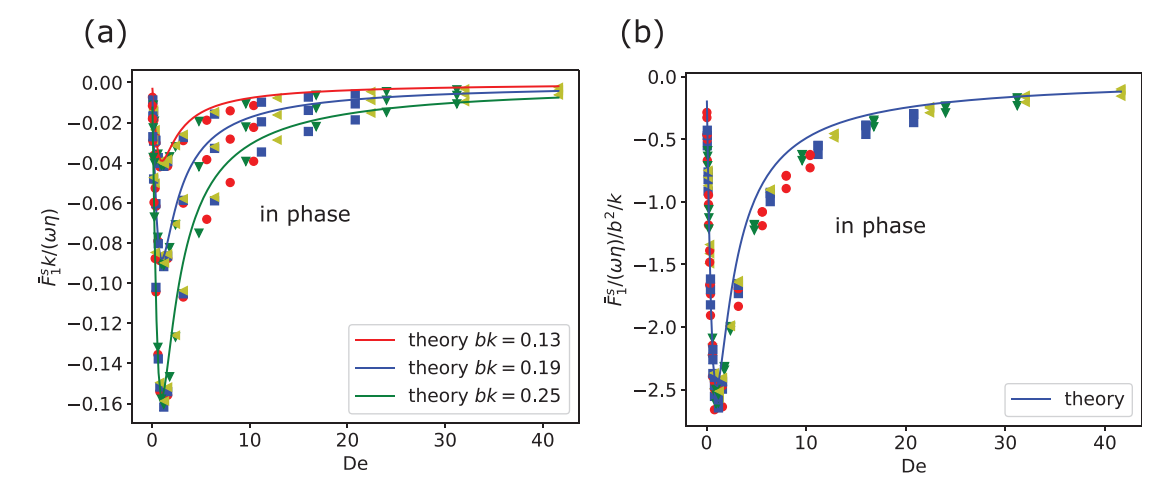


FIG. 9. Synchronization force amplitudes of two waving sheets (prescribed actuation) in viscoelastic fluids. (a) $\bar{F}_1^s k/(\omega \eta)$ and (b) $\bar{F}_1^s/(\omega \eta b^2 k)$ as a function of De for various bk. Different simulation datasets are plotted by symbols, corresponding to $\omega=0.4$ (red circles); $\omega=0.8$ (blue squares); $\omega=1.2$ (green down-pointing triangles); and $\omega=1.6$ (yellow left-pointing triangles). Solid lines are theoretical predictions³¹ from Eq. (18). Here, $\eta_s/\eta=0.1875$, $\eta_s/\eta_{ref}=0.9375$, and $\rho/\rho_{ref}=0.064$ are fixed in all simulations.

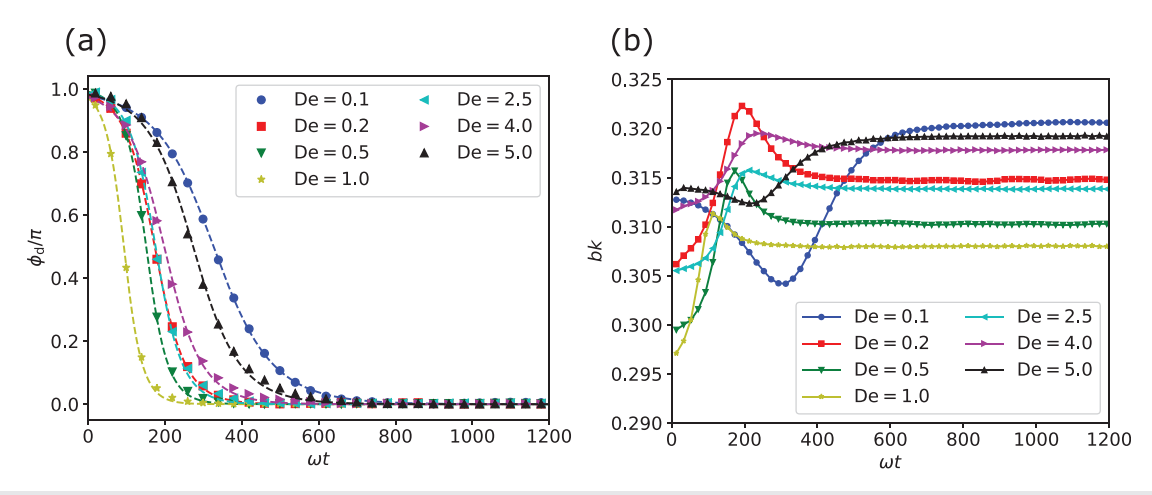


FIG. 10. Dynamic synchronization of two flexible sheets mediated by fluid viscoelasticity. (a) Phase difference $\phi_{\rm d}$ as a function of time for different De. Dashed lines represent fits using Eq. (15). (b) Beating wave amplitudes. Here, $\eta_{\rm s}/\eta=0.1875$, $\eta_{\rm s}/\eta_{\rm ref}=0.9375$, $\rho/\rho_{\rm ref}=0.125$, $\omega=0.5$, $\theta_{\rm b}/\pi=0.056$, $\kappa/\kappa_{\rm ref}=28.125$, and $\rho_{\rm 0}/\rho_{\rm ref}=640$.

accurate. Interestingly, the synchronization times in viscoelastic fluids have similar magnitudes as those in Newtonian fluids (compare with Figs. 6 and 7).

According to the theoretical prediction in Eq. (18),³¹ the synchronization forces resulting from fluid viscoelasticity are of the order $\mathcal{O}(b^2k^2)$, which is similar to the synchronization forces originating from inertial effects, see Eq. (13). Therefore, it is plausible to expect the transition from in-phase to opposite-phase configuration with increasing Re in viscoelastic fluids. Figure 11 illustrates the competing effects of viscoelasticity and inertia characterized by a dimensionless parameter $\text{Re}(1+\text{De}^2)/\text{De}$. This definition is motivated by Eq. (13), where the synchronization force due to fluid inertia is proportional to $\rho\omega b^2/k$, and by Eq. (18) with $\bar{F}^s\sim\omega\eta \text{De}/(1+\text{De}^2)/k$ due to

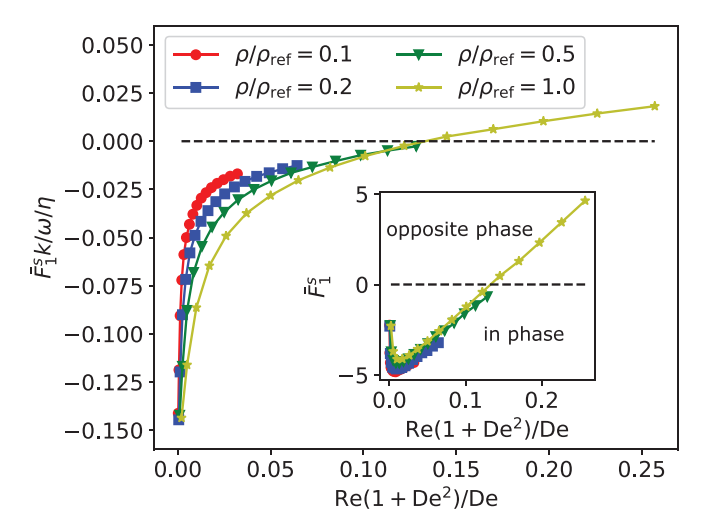


FIG. 11. Synchronization force amplitudes of two waving sheets in viscoelastic fluids for different $\rho/\rho_{\rm ref} \in [0.125,1]$, affecting the value of Re, and for different $\omega \in [0.1,1.6]$, changing the value of De. The inset shows that \overline{F}_1^s fall nearly onto a single curve when presented as a function of Re(1 + De²)/De. Other parameters bk = 0.17, $\eta_{\rm s}/\eta = 0.375$, $\eta_{\rm s}/\eta_{\rm ref} = 1.875$, and $\rho_0/\rho_{\rm ref} = 640$ remain fixed.

viscoelasticity. As shown in the inset of Fig. 11, the resultant synchronization forces for different ρ (affecting the value of Re) and ω (affecting the value of De) fall approximately onto a single curve as a function of Re(1 + De²)/De. Clearly, the in-phase to opposite-phase transition occurs at large enough Re(1 + De²)/De values. Interestingly, this transition can be triggered not only by increasing Re, but also by increasing De provided that De \gg 1. This can be rationalized by the fact that when ω is fixed, viscoelastic synchronization forces asymptotically approach zero with increasing De [see Eq. (18)].

The prediction that synchronization of two sheets with a fixed ω is weak at large De seemingly disagrees with recent experimental³⁴ and numerical⁵⁶ studies on sperm interaction, which demonstrate that fluid viscoelasticity can significantly enhance clustering. Note that the theoretical prediction by Taylor¹⁷ in Eq. (10) is of the order $\mathcal{O}(b^4k^4)$ and has been shown to be accurate for $bk \leq 0.4$.⁵⁷ The theoretical prediction in Eq. (18) for Oldroyd-B fluids³¹ is of the order $\mathcal{O}(b^2k^2)$, such that it is reliable for small bk as verified by our simulations in Fig. 9, but is expected to be less accurate for large bk values. Furthermore, there exist a number of experimental studies 9,10,34,52 with flagellated microswimmers, whose wave amplitude is large enough to make the assumption of small bk invalid. Figure 12 shows synchronization force amplitudes of two waving sheets in viscoelastic fluids for bk = 0.5, bk = 0.63, and bk = 0.75. The simulation parameters here are the same as those in Fig. 9. Clearly, the simulated $\bar{\bar{F}}_1^s$ values for large bk are significantly larger than those predicted theoretically at large De. This demonstrates that for bk > 0.4, fluid viscoelasticity plays a much more prominent role for sheet synchronization than predicted theoretically for small bk. Interestingly, the dependence of \bar{F}_1^s on bk > 0.4 has an exponent that can be significantly larger than two. For comparison, an increase in the synchronization force for Newtonian fluids at large enough Re and bk > 0.4 is proportional to b^2 , as shown in Fig. 5. Therefore, our simulations demonstrate that fluid viscoelasticity is the main cause of a tremendous increase in synchronization forces at large bk and De, providing a plausible explanation for the enhanced clustering of flagellated microswimmers in viscoelastic fluids.

Note that the Oldroyd-B model becomes unphysical when the Weissenberg number, which relates fluid relaxation time to the time determined by a characteristic strain rate, approaches Wi ≈ 1 . As a precautionary step, the Oldroyd-B model has been tested using Kolmogorov flow, leading to accurate results for Wi ≤ 0.8 , while for Wi ≥ 0.9 the SDPD simulations become unstable. For the synchronization problem of two sheets, Weissenberg number can be defined as Wi = $\tau b/(\lambda/f) = bk\omega\tau/(2\pi)^2$ with $f = \omega/(2\pi)$. For example, simulation results in Fig. 9 agree well with the analytical solution in Eq. (18) and correspond to Wi $\in [2.5 \times 10^{-4}, 0.26]$ for bk = 0.25. For comparison, Wi $\in [5 \times 10^{-4}, 0.41]$ for bk = 0.5 in Fig. 12(a), Wi $\in [6.4 \times 10^{-4}, 0.36]$ for bk = 0.63 in Fig. 12(b), and Wi $\in [7.6 \times 10^{-4}, 0.24]$ for bk = 0.75 in Fig. 12(c). Therefore, all presented results are well within the limit of Oldroyd-B model applicability, confirming that the dramatic increase in synchronization forces at large De and bk is not due to any model shortcomings.

C. Swimming efficiency of two synchronized sheets

Different mechanisms, such as inertia, sheet elasticity, and fluid compressibility and viscoelasticity, can contribute to the synchronization of two sheets. An interesting question is whether the behavior of two synchronized sheets is different from that of a single sheet. In the early work of Taylor, ¹⁷ it has been shown that energy dissipation of two sheets at Re=0 is minimized (maximized) when they attain the in-phase (opposite-phase) configuration. More recent theoretical study²⁵ reports that the stable synchronized phase is not necessarily the phase with a minimum energy dissipation. There exist numerous examples of biological microorganisms swimming in clusters, suggesting that collective swimming may have some advantages. A numerical study about sperm swimming⁶ reports that clustered sperms swim slower, and consume a lower amount of energy per sperm than a single one alone. However, it is not clear whether different factors (e.g., inertia, sheet elasticity, and fluid viscoelasticity) affect the properties of synchronized sheets in a qualitatively similar way.

Figure 13 compares output power, swimming velocity, and efficiency of a pair of synchronized sheets with those of a single sheet. In these simulations, two sheets are let to fully synchronize, and after that the aforementioned measurements are performed. Three different synchronization factors are considered, including sheet synchronization dominated by inertial effects (denoted as "IN"), sheet elasticity (abbreviated as "SE"), and fluid viscoelasticity (denoted by "VE").

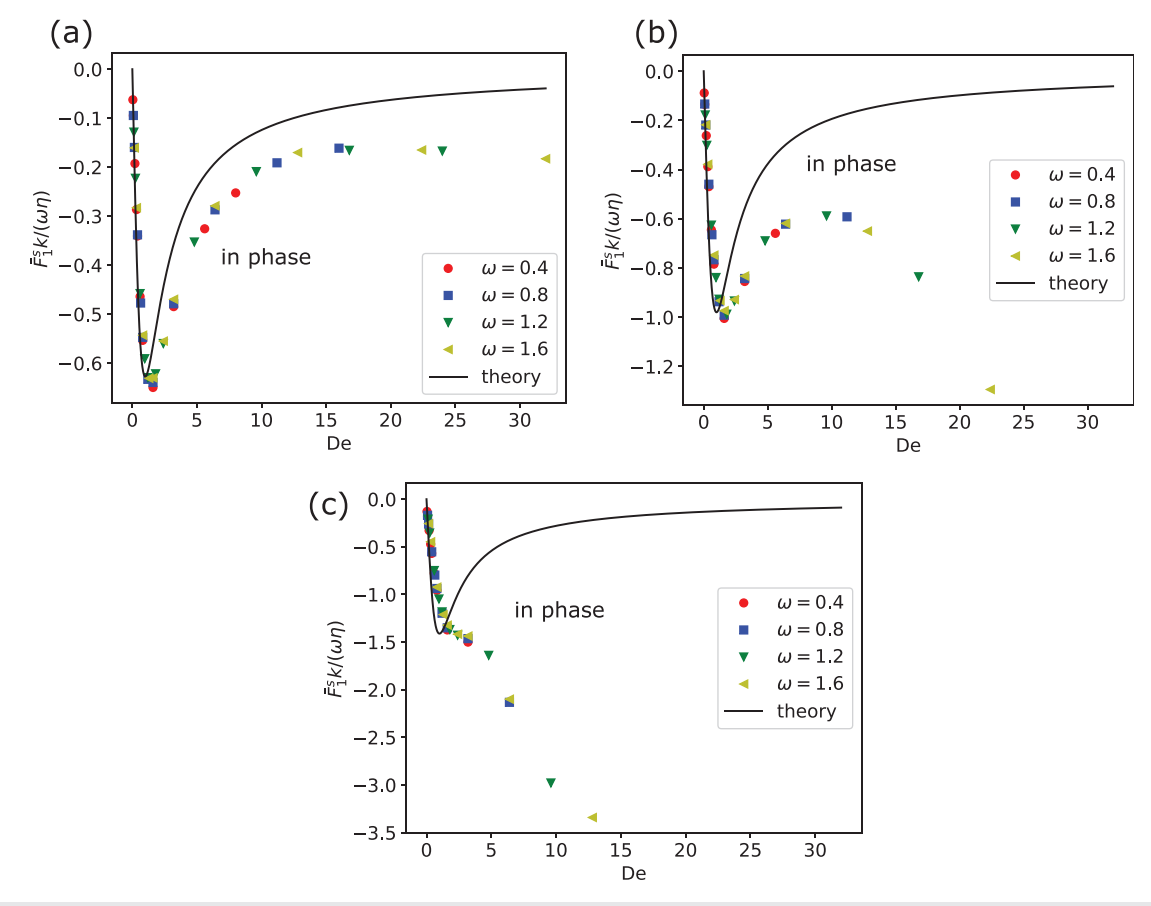


FIG. 12. Synchronization force amplitudes as a function of De for (a) bk=0.5, (b) bk=0.63, and (c) bk=0.75. As bk is increased, synchronization forces strongly increase at large enough De. Note that for large bk, the dependence of F^s on phase difference ϕ_d is no longer a sine function. Therefore, \bar{F}_1^s corresponds to the maximum of $F_1^s(\phi_d)$ here. Other parameters $\eta_s/\eta=0.1875$, $\eta_s/\eta_{ref}=0.9375$, $\rho/\rho_{ref}=0.064$, and $\rho_0/\rho_{ref}=640$ remain fixed. In all cases, $Re(1+De^2)/De\ll 1$.

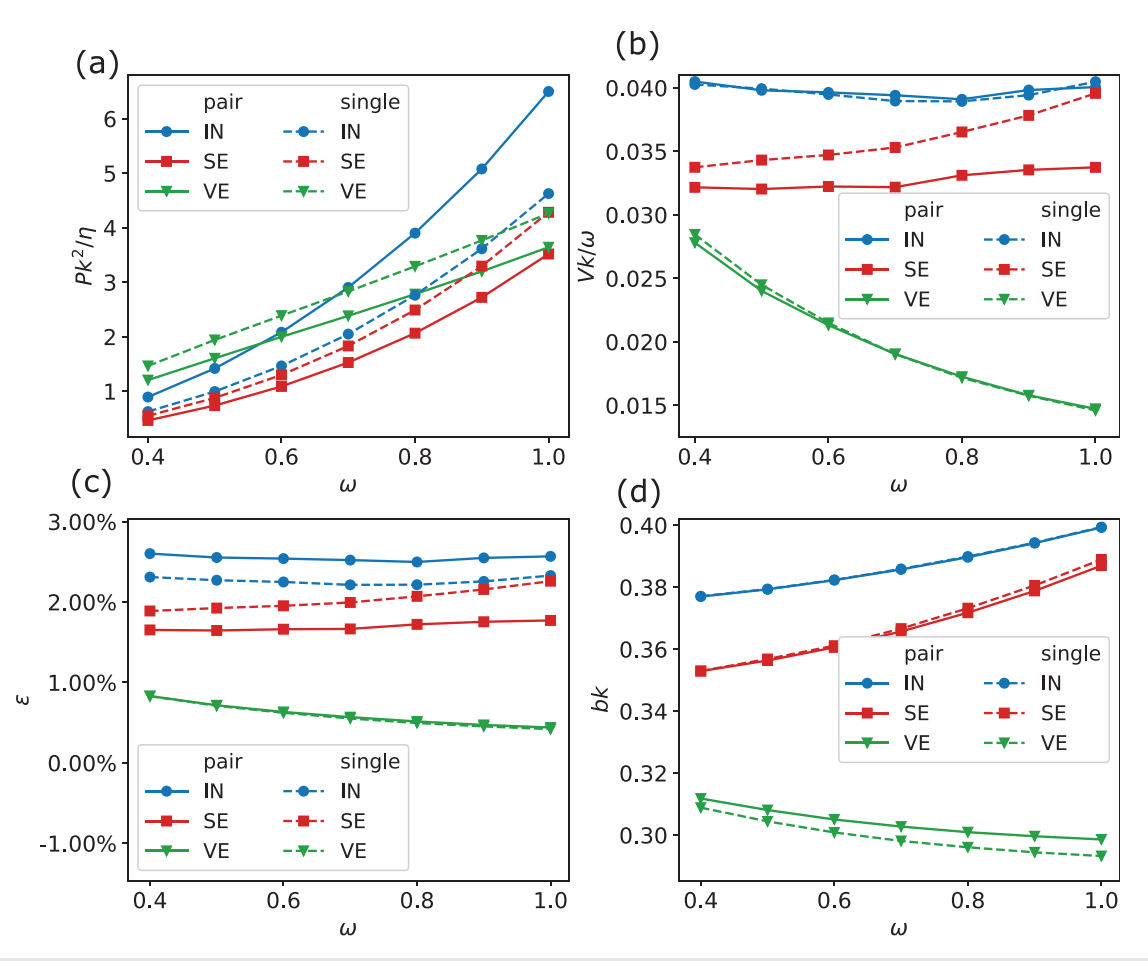


FIG. 13. Swimming properties of two synchronized sheets in comparison with a single sheet. (a) Sheet output power P, (b) swimming velocity V, (c) swimming efficiency \mathscr{E} , and (d) beating amplitude b for various conditions. The abbreviation "IN" denotes Newtonian-fluid simulations, in which inertial effects dominate, with the following parameters $\eta/\eta_{\rm ref}=0.5$, $\theta_b/\pi=0.044$, $\kappa/\kappa_{\rm ref}=20.63$, and $p_0/p_{\rm ref}=256$. The abbreviation "SE" denotes Newtonian-fluid simulations, in which the effect of sheet flexibility dominates, with simulations parameters $\theta_b/\pi=0.028$, $\kappa/\kappa_{\rm ref}=15.86$, and $p_0/p_{\rm ref}=256$. "VE" corresponds to non-Newtonian-fluid simulations with dominating viscoelastic effects for simulation parameters $\eta_s/\eta=0.1875$, $\eta_s/\eta_{\rm ref}=0.9375$, $\rho/\rho_{\rm ref}=0.125$, $\theta_b/\pi=0.056$, $\kappa/\kappa_{\rm ref}=28.125$, and $p_0/p_{\rm ref}=640$.

Figure 13(a) presents total output power for the three cases, which is computed as $P = -\sum_{i \leq N} \sum_{j \leq M} F_{ij} \cdot \mathbf{v}_i$, where N is the total number of sheet particles, M is the total number of fluid particles, and F_{ij} are interparticle forces. Note that only for the inertia-dominated case, the output power of a synchronized pair is larger than that of a single sheet. This is due to the fact that the sheets synchronize to the opposite-phase conformation, for which the dissipation energy is largest in Stokes flow regime (Re here is smaller than 0.04). Interestingly, swimming velocities of a synchronized pair and a single sheet do not differ much, see Fig. 13(b). Only in the "SE" case, the swimming velocity of a single sheet is slightly larger than that of the pair. These results indicate that only in the "VE" case, the synchronized pair of sheets swims not slower than the corresponding single sheet, and has a lower output power.

Figure 13(c) presents swimming efficiency $\mathscr{E} = P_{\rm eff}/P$ for different cases, where $P_{\rm eff} = -F_x^{\rm drag} V_x$ is the effective power with $F_x^{\rm drag}$ being the x component of drag forces exerted by the fluid on the sheets and V_x is the swimming speed. Note that the total force exerted by fluid on a swimmer is always zero, but it can be divided into propulsive

and drag components. The propulsive component is due to normal stresses, while the drag component corresponds to tangential stresses. In the case of dominating inertial effects, the swimming efficiency (about 2%-3%) is largest, and the synchronized pair is slightly more efficient than a single sheet. In case when sheet-elasticity effects dominate, the pair has a lower efficiency than the single sheet. Finally, in the case of dominating viscoelastic contributions, the swimming efficiency is smallest and there is no difference in \mathscr{E} for the synchronized pair and single sheet. Nevertheless, swimming efficiency may not be an appropriate measure to clearly determine possible advantages/disadvantages of synchronized swimming. For example, for the "IN" case in Fig. 13, the efficiency and total output power are larger for the synchronized pair than for the single sheet, but the swimming speed is nearly the same. In this case, the sheets synchronize toward the opposite-phase configuration, which results in a relatively strong backward (peristalticlike) flow between them, thus increasing the resistance for swimming. Finally, Fig. 13(d) shows that wave amplitudes are nearly the same for both the synchronized pair and single sheet in all cases.

TABLE II. Different factors which lead to the synchronization of two sheets toward the in-phase or opposite-phase configurations. When several factors are present, the final configuration is determined by their competition.

Factors	Theory	Simulation
No inertia (Re = 0)	No synchronization (incompressible fluid, inextensible sheets) ²⁵	
Inertia (Re > 0)		Opposite-phase configuration (this study and Ref. 28)
Asymmetric wave	In-phase or opposite-phase configuration, depending on the asymmetry $(Re = 0)^{25,27}$	
Sheet flexibility	In-phase configuration $(Re = 0)^{30}$	In-phase configuration (Re > 0, this study)
Fluid compressibility		In-phase configuration (Re > 0, this study)
Fluid viscoelasticity	In-phase configuration ³¹	In-phase configuration (this study and Ref. 32)

IV. CONCLUSIONS

We have employed numerical simulations to study the effect of inertia, sheet flexibility, and fluid compressibility and viscoelasticity on the synchronization of two inextensible or flexible sheets. Table II shows the summary of all results. Inertial effects always lead to sheet synchronization toward the opposite-phase configuration. When inertial effects dominate, the synchronization time τ^s of two sheets is inversely proportional to the Reynolds number, such that $\tau^s \omega \propto \text{Re}^{-1}$. Both fluid compressibility and sheet flexibility drive synchronization toward the inphase configuration, and compete with inertial effects for Re > 0. Furthermore, we have systematically tested the theoretical prediction³¹ of the synchronization forces between two sheets in viscoelastic fluids, favoring the in-phase configuration. Our simulation results are in excellent agreement with the theoretical prediction for bk < 0.4; however, for large bk, synchronization forces strongly depart from the theory for De > 1, indicating a rapid synchronization. Thus, for De > 1 and large enough bk, fluid viscoelasticity has a dramatic effect on the synchronization of two sheets, which clearly dominates over other factors, such as inertia and sheet elasticity. This result is consistent with the observations of significant enhancement of sperm clustering in viscoelastic fluids. 34 Finally, sheet synchronization dominated by fluid viscoelasticity does not impede swimming velocity of the synchronized pair, but has a lower output power in comparison

Simulation results presented here constitute a systematic study of competing effects for the synchronization of two sheets. They can be used to qualitatively assess the importance of possible factors for experimentally observed interactions between biological microswimmers or artificial microrobots. This knowledge is useful for a better understanding of collective behavior of microswimmers and for tuning of synchronization interactions between artificial microrobots.

ACKNOWLEDGMENTS

C.M. acknowledges the funding by the China Scholarship Council (CSC) and German Academic Exchange Service (DAAD) through the Sino-German (CSC-DAAD) Postdoc Scholarship Program. We gratefully acknowledge the computing time granted through JARA-HPC on the supercomputer JURECA⁵⁸ at Forschungszentrum Jülich.

APPENDIX: CALCULATION OF FLEXURAL RIGIDITY κ

We consider a ring (see Fig. 14) whose structure is similar to the sheet in Fig. 1(b). In continuum, elastic energy of the ring is given by

$$E = \frac{\kappa}{2} \int_{2\pi R} \frac{\mathrm{d}l}{R^2} = \frac{\pi \kappa}{R},\tag{A1}$$

which can be compared with the energy of a discrete structure. The force balance at O_1 yields

$$2\zeta_{\rm s}(l_1 - l_0)\sin\frac{\theta}{2} = 2\zeta_{\rm s}\left(\frac{\sqrt{5}}{2}l_0 - l_2\right)\cdot\frac{2}{\sqrt{5}},$$
 (A2)

resulting in

$$l_2 \approx \frac{\sqrt{5}}{2} \left(l_0 - \Delta l \frac{\theta}{2} \right),$$
 (A3)

with $\Delta l = l_1 - l_0$. Under the assumption that the middle layer does not deform, the force balance at O_2 leads to $l_2 = l_3$. From the discrete geometry in Fig. 14, we obtain

$$\frac{R}{l_0} = \frac{R + \frac{2}{\sqrt{5}} l_2}{l_0 + \Delta l} \quad \Rightarrow \quad \Delta l = \frac{2l_0^2 R}{2R^2 + l_0^2}.$$
 (A4)

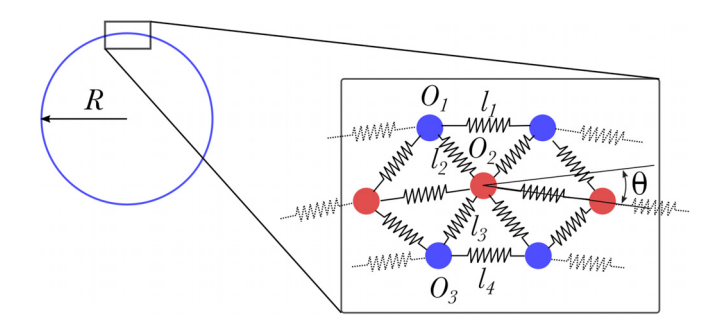


FIG. 14. Schematic of a ring used for the calculation of sheet flexural rigidity κ . R is the ring radius, l_1, \ldots, l_4 are lengths of the corresponding springs, and θ is the angle between two adjacent springs in the middle layer. Equilibrium lengths are $l_1^0 = l_0^1 = l_0^1$

Then, the elastic energy of the discrete structure is given by

$$E_d = N\zeta_s \left(\Delta l^2 + \frac{5}{8} \Delta l^2 \theta^2 \right) + N \frac{\zeta_\theta}{2} \theta^2. \tag{A5}$$

By substituting Δl and $\theta = l_0/R$ into the equation above, we obtain

$$E_d \approx \frac{2\pi\zeta_s l_0^3 + \pi\zeta_\theta l_0}{R},\tag{A6}$$

which results, when compared with Eq. (A1), in the expression for flexural rigidity κ as

$$\kappa = 2\zeta_s l_0^3 + \zeta_\theta l_0. \tag{A7}$$

DATA AVAILABILITY

The data are available from the corresponding author upon reasonable request.

REFERENCES

- ¹E. Lauga and T. R. Powers, "The hydrodynamics of swimming microorganisms," Rep. Prog. Phys. **72**, 096601 (2009).
- ²J. Elgeti, R. G. Winkler, and G. Gompper, "Physics of microswimmers single particle motion and collective behavior: A review," Rep. Prog. Phys. 78, 056601 (2015).
- ³C. Bechinger, R. Di Leonardo, H. Löwen, C. Reichhardt, G. Volpe, and G. Volpe, "Active particles in complex and crowded environments," Rev. Mod. Phys. 88, 045006 (2016).
- ⁴S. Palagi and P. Fischer, "Bioinspired microrobots," Nat. Rev. Mater. 3, 113–124 (2018).
- ⁵L. J. Fauci and A. McDonald, "Sperm motility in the presence of boundaries," Bull. Math. Biol. **57**, 679–699 (1995).
- ⁶Y. Yang, J. Elgeti, and G. Gompper, "Cooperation of sperm in two dimensions: Synchronization, attraction, and aggregation through hydrodynamic interactions," Phys. Rev. E 78, 061903 (2008).
- ⁷D. D. Olson and L. J. Fauci, "Hydrodynamic interactions of sheets vs filaments: Synchronization, attraction, and alignment," Phys. Fluids 27, 121901 (2015).
- ⁸I. Llopis, I. Pagonabarraga, M. Cosentino Lagomarsino, and C. P. Lowe, "Cooperative motion of intrinsic and actuated semiflexible swimmers," Phys. Rev. E 87, 032720 (2013).
- ⁹D. M. Woolley, R. F. Crockett, W. D. I. Groom, and S. G. Revell, "A study of synchronisation between the flagella of bull spermatozoa, with related observations," J. Exp. Biol. 212, 2215–2223 (2009).
- ¹⁰R. Nosrati, A. Driouchi, C. M. Yip, and D. Sinton, "Two-dimensional slither swimming of sperm within a micrometre of a surface," Nat. Commun. 6, 8703 (2015).
- ¹¹N. Taketoshi, T. Omori, and T. Ishikawa, "Elasto-hydrodynamic interaction of two swimming spermatozoa," Phys. Fluids 32, 101901 (2020).
- ¹²M.-J. Kim, J. C. Bird, A. J. Van Parys, K. S. Breuer, and T. R. Powers, "A macroscopic scale model of bacterial flagellar bundling," Proc. Natl. Acad. Sci. U. S. A. 100, 15481–15485 (2003).
- ¹³S. Y. Reigh, R. G. Winkler, and G. Gompper, "Synchronization and bundling of anchored bacterial flagella," Soft Matter 8, 4363–4372 (2012).
- ¹⁴D. R. Brumley, M. Polin, T. J. Pedley, and R. E. Goldstein, "Hydrodynamic synchronization and metachronal waves on the surface of the colonial alga Volvox carteri," Phys. Rev. Lett. 109, 268102 (2012).
- ¹⁵J. Elgeti and G. Gompper, "Emergence of metachronal waves in cilia arrays," Proc. Natl. Acad. Sci. U. S. A. 110, 4470–4475 (2013).
- ¹⁶H. Guo, L. Fauci, M. Shelley, and E. Kanso, "Bistability in the synchronization of actuated microfilaments," J. Fluid Mech. 836, 304–323 (2018).
- ¹⁷G. I. Taylor, "Analysis of the swimming of microscopic organisms," Proc. R. Soc. London, Ser. A 209, 447–461 (1951).
- ¹⁸D. R. Brumley, K. Y. Wan, M. Polin, and R. E. Goldstein, "Flagellar synchronization through direct hydrodynamic interactions," eLife 3, e02750 (2014).

- ¹⁹T. J. Pedley and J. O. Kessler, "Hydrodynamic phenomena in suspensions of swimming microorganisms," Annu. Rev. Fluid Mech. 24, 313–358 (1992).
- 20R. Golestanian, J. M. Yeomans, and N. Uchida, "Hydrodynamic synchronization at low Reynolds number," Soft Matter 7, 3074–3082 (2011).
- ²¹A. J. Reynolds, "The swimming of minute organisms," J. Fluid Mech. 23, 241–260 (1965).
- ²²E. O. Tuck, "A note on a swimming problem," J. Fluid Mech. 31, 305–308
- 23 E. Diller, J. Zhuang, G. Z. Lum, M. R. Edwards, and M. Sitti, "Continuously distributed magnetization profile for millimeter-scale elastomeric undulatory swimming," Appl. Phys. Lett. 104, 174101 (2014).
- ²⁴H.-W. Huang, M. S. Sakar, A. J. Petruska, S. Pané, and B. J. Nelson, "Soft micromachines with programmable motility and morphology," Nat. Commun. 7, 12263 (2016).
- ²⁵G. J. Elfring and E. Lauga, "Hydrodynamic phase locking of swimming microorganisms," Phys. Rev. Lett. 103, 088101 (2009).
- ²⁶B. Friedrich, "Hydrodynamic synchronization of flagellar oscillators," Eur. Phys. J.: Spec. Top. 225, 2353–2368 (2016).
- ²⁷G. J. Elfring and E. Lauga, "Passive hydrodynamic synchronization of two-dimensional swimming cells," Phys. Fluids 23, 011902 (2011).
- ²⁸L. J. Fauci, "Interaction of oscillating filaments: A computational study," J. Comput. Phys. 86, 294–313 (1990).
- ²⁹M. Theers and R. G. Winkler, "Synchronization of rigid microrotors by time-dependent hydrodynamic interactions," Phys. Rev. E 88, 023012 (2013).
- ³⁰G. J. Elfring and E. Lauga, "Synchronization of flexible sheets," J. Fluid Mech. 674, 163–173 (2011).
- ³¹G. J. Elfring, O. S. Pak, and E. Lauga, "Two-dimensional flagellar synchronization in viscoelastic fluids," J. Fluid Mech. 646, 505–515 (2010).
- ³²J. C. Chrispell, L. J. Fauci, and M. Shelley, "An actuated elastic sheet interacting with passive and active structures in a viscoelastic fluid," Phys. Fluids 25, 013103 (2013).
- ³³C. Mettot and E. Lauga, "Energetics of synchronized states in three-dimensional beating flagella," Phys. Rev. E 84, 061905 (2011).
- ³⁴C.-K. Tung, C. Lin, B. Harvey, A. G. Fiore, F. Ardon, M. Wu, and S. S. Suarez, "Fluid viscoelasticity promotes collective swimming of sperm," Sci. Rep. 7,
- 35P. Español and M. Revenga, "Smoothed dissipative particle dynamics," Phys. Rev. E 67, 026705 (2003).
- ³⁶K. Müller, D. A. Fedosov, and G. Gompper, "Smoothed dissipative particle dynamics with angular momentum conservation," J. Comput. Phys. 281, 301–315 (2015).
- 37 A. Vázquez-Quesada, M. Ellero, and P. Español, "Smoothed particle hydrodynamic model for viscoelastic fluids with thermal fluctuations," Phys. Rev. E 79, 056707 (2009).
- ³⁸J. J. Monaghan, "Smoothed particle hydrodynamics," Annu. Rev. Astron. Astrophys. 30, 543–574 (1992).
- 39P. J. Hoogerbrugge and J. M. V. A. Koelman, "Simulating microscopic hydrodynamic phenomena with dissipative particle dynamics," Europhys. Lett. 19, 155–160 (1992).
- ⁴⁰P. Español and P. Warren, "Statistical mechanics of dissipative particle dynamics," Europhys. Lett. 30, 191–196 (1995).
- ⁴¹X. Y. Hu and N. A. Adams, "Angular-momentum conservative smoothed particle dynamics for incompressible viscous flows," Phys. Fluids 18, 101702 (2006).
- ⁴²I. O. Götze, H. Noguchi, and G. Gompper, "Relevance of angular momentum conservation in mesoscale hydrodynamics simulations," Phys. Rev. E 76, 046705 (2007).
- 43M. P. Allen and D. J. Tildesley, Computer Simulation of Liquids (Clarendon Press, New York, 1991).
- ⁴⁴L. B. Lucy, "A numerical approach to the testing the fission hypothesis," Astron. J. 82, 1013–1024 (1977).
- 45E. Lauga, "Propulsion in a viscoelastic fluid," Phys. Fluids 19, 083104 (2007).
- 46J. P. Morris, P. J. Fox, and Y. Zhu, "Modeling low Reynolds number incompressible flows using SPH." J. Comput. Phys. 136, 214–226 (1997).
- pressible flows using SPH," J. Comput. Phys. 136, 214–226 (1997).

 47 L. D. G. Sigalotti, J. Klapp, E. Sira, Y. Meleán, and A. Hasmy, "SPH simulations of time-dependent Poiseuille flow at low Reynolds numbers," J. Comput. Phys. 191, 622–638 (2003).

- ⁴⁸M. Meister, G. Burger, and W. Rauch, "On the Reynolds number sensitivity of smoothed particle hydrodynamics," J. Hydraul. Res. 52, 824–835 (2014).
- ⁴⁹G. J. Elfring and E. Lauga, "Theory of locomotion through complex fluids," in *Complex Fluids in Biological Systems*, edited by S. E. Spagnolie (Springer, New York, NY, 2015), pp. 283–317.
- 50 T. R. Ives and A. Morozov, "The mechanism of propulsion of a model micro-swimmer in a viscoelastic fluid next to a solid boundary," Phys. Fluids 29, 121612 (2017).
- 51 E. A. Gaffney, H. Gadélha, D. J. Smith, J. R. Blake, and J. C. Kirkman-Brown, "Mammalian sperm motility: Observation and theory," Annu. Rev. Fluid Mech. 43, 501–528 (2011).
- ⁵²G. Saggiorato, L. Alvarez, J. F. Jikeli, U. B. Kaupp, G. Gompper, and J. Elgeti, "Human sperm steer with second harmonics of the flagellar beat," Nat. Commun. 8, 1415 (2017).
- ⁵³S. K. Lai, Y.-Y. Wang, D. Wirtz, and J. Hanes, "Micro- and macrorheology of mucus," Adv. Drug Delivery Rev. 61, 86–100 (2009).
- 54R. Adler, "A study of locking phenomena in oscillators," Proc. IRE 34, 351–357 (1946).
- 55T. Niedermayer, B. Eckhardt, and P. Lenz, "Synchronization, phase locking, and metachronal wave formation in ciliary chains," Chaos 18, 037128 (2008).
- ⁵⁶K. Ishimoto and E. A. Gaffney, "Hydrodynamic clustering of human sperm in viscoelastic fluids," Sci. Rep. 8, 15600 (2018).
- 57 M. Sauzade, G. J. Elfring, and E. Lauga, "Taylor's swimming sheet: Analysis and improvement of the perturbation series," Phys. D 240, 1567–1573 (2011).
- 58\u00e4ilich Supercomputing Centre, "JURECA: Modular supercomputer at J\u00fclich Supercomputing Centre," J. Large-Scale Res. Facil. 4, A132 (2018).